

# Structual Study of Galactic Hot Gas toward Markarian 421 from X-Ray Absorption and Emission Lines

Kazuhiro SAKAI,<sup>1</sup> Yangsen YAO,<sup>2</sup> Kazuhisa MITSUDA,<sup>1</sup> Noriko YAMASAKI,<sup>1</sup> Q. Daniel WANG,<sup>3</sup> Yoh TAKEI,<sup>1</sup>  
and Dan MCCAMMON<sup>4</sup>

<sup>1</sup>*Institute of Space and Astronautical Science, Japan Aerospace Exploration Agency, 3-1-1 Yoshinodai, Chuo, Sagamihara, Kanagawa 252-5210, Japan*

<sup>2</sup>*Eureka Scientific, Inc., 2452 Delmer Street Suite 100, Oakland, CA 94602, USA*

<sup>3</sup>*Department of Astronomy, University of Massachusetts, Amherst, MA 01003, USA*

<sup>4</sup>*Department of Physics, University of Wisconsin, Madison, 1150 University Avenue, Madison, WI 53706, USA*  
*sakai@astro.isas.jaxa.jp*

(Received ; accepted )

## Abstract

We present a structural study of the hot ISM in the Galactic halo along the sight line toward the bright active galactic nucleus Mkn 421. The O VII and O VIII absorption lines were measured with the Low Energy Transmission Grating Spectrograph aboard *Chandra* toward Mkn 421, and the O VII and O VIII emission lines were observed in the adjacent fields of the sight line with the X-ray Imaging Spectrometer aboard *Suzaku*. We jointly analyzed the absorption and the emission spectra assuming exponential distributions of the gas temperature and density from the Galactic plane, and constrained the temperature and density at the plane to be  $(3.2^{+0.6}_{-0.7}) \times 10^6$  K and  $(1.2^{+0.5}_{-0.4}) \times 10^{-3} \text{ cm}^{-3}$ , with the scale heights of  $1.6^{+1.7}_{-0.7}$  kpc and  $> 2.8$  kpc respectively. The results are consistent with those obtained in the LMC X-3 direction and the PKS 2155–304 direction, describing a thick disk-like hot gas with its height of a few kpc from the Galactic plane.

**Key words:** Galaxy: disk - Galaxy: halo - X-rays: diffuse background - X-rays: ISM

## 1. Introduction

The observation of the whole sky in the soft X-ray band, especially between 0.5 and 1 keV, has clearly showed not only enhanced emission from regions such as the Galactic Center and the North Polar Spur, but also a dimmer yet gleaming diffuse background in almost all

directions. This diffuse X-ray background is considered to be produced by a combination of several sources, and a clean separation of them has been a difficult task.

McCammon et al. (2002) showed that about 40% of the dimmer all-sky diffuse emission in the 0.5 – 1.0 keV band can be attributed to the extragalactic contribution, which we refer to as the Cosmic X-ray Background (CXB) in this paper. The remainder of the emission can be characterized by highly ionized ion emission lines, which are considered to originate from at least three different sources; the solar-wind charge-exchange (SWCX)-induced emission from the Heliosphere (Cox 1998; Cravens 2000; Lallement et al. 2004), the thermal emission from the hot gas in local hot bubble (LHB) (McCammon & Sanders 1990), and another thermal emission from a thick Galactic hot gaseous disk (Yao & Wang 2007; Yoshino et al. 2009; Yao et al. 2009; Hagihara et al. 2010). The first two sources are considered to arise from the local part of the Galaxy and are hard to be separated from each other. The sum of these emission components can be approximated by an optically-thin thermal plasma of  $kT \sim 0.1$  keV with negligible foreground absorption (Smith et al. 2007; Henley et al. 2007; Galeazzi et al. 2007; Kuntz & Snowden 2008; Masui et al. 2009).

The last component is considered to arise from distant parts of the Galaxy; mostly beyond the bulk of absorption in the Galactic disk. The spectrum of the component can be described by thermal plasma of a temperature of 0.25 keV. There is so far little constraint on the distances other than their foreground absorption. The detection of highly ionized absorption lines of O VII, O VIII, and/or Ne IX in spectra of Galactic sources (e.g., Futamoto et al. 2004; Yao & Wang 2005; Juett et al. 2006; Yao et al. 2008) indicates that a large fraction of hot gas contributing to the absorption exists within distance scales of  $\sim 10$  kpc.

Yao & Wang (2007) introduced a joint fitting method of the high-resolution absorption and emission spectra to constrain not only the temperature but also the extent and density of the hot gaseous disk. In the work by Yao & Wang, the high-resolution absorption spectrum observed with *Chandra* is jointly fitted with the broadband emission spectrum from the Rosat All Sky Survey (RASS) of the field adjacent to the sight line toward the nearby bright active galactic nucleus Mkn 421. This joint fit provides tight constraints on the extent and density of the hot gas, which is shown to be in a nonisothermal state, as evidenced by the mean temperature differences inferred from fitting the absorption and emission spectra independently. The joint fit then assumes a model of hot gas distribution with the temperature and density decreasing exponentially with the vertical distance from the Galactic plane. This exponential model was also used in the joint analysis of the *Chandra* observed absorption spectrum along the sight line toward the LMC X-3 with the *Suzaku* observed emission spectra in the adjacent fields (Yao et al. 2009). This analysis gives the estimates of the temperature and density at the Galactic plane as  $(3.6_{-0.7}^{+0.8}) \times 10^6$  K and  $(1.4_{-1.0}^{+2.0}) \times 10^{-3}$  cm $^{-3}$  and the exponential scale heights of the hot gas as  $1.4_{-1.2}^{+3.8}$  kpc and  $2.8_{-1.8}^{+3.6}$  kpc, respectively.

Furthermore, Hagihara et al. (2010) applied the same model along the sight line toward

the blazar PKS 2155–304, and estimated the gas temperature and density at the Galactic plane as  $(2.5_{-0.3}^{+0.6}) \times 10^6$  K and  $(1.4_{-0.4}^{+0.5}) \times 10^{-3}$  cm $^{-3}$  with the exponential scale heights of the hot gas as  $5.6_{-4.2}^{+7.4}$  kpc and  $2.3_{-0.8}^{+0.9}$  kpc, respectively, which are consistent with those for the LMC X–3 direction. Both results from Yao et al. (2009) and Hagihara et al. (2010) suggested the presence of a thick hot gaseous disk with the scale height less than 10 kpc that is consistent with the Galactic source absorption lines.

The Galactic hot gaseous disk has also been studied for a possibility of its being a reservoir of missing baryons in the local universe (Gupta et al. 2012; Gupta et al. 2013; Fang et al. 2013; Miller et al. 2013). It is therefore essential to constrain the scale heights of the hot gas in different parts of the sky individually. Gupta et al. (2012) have argued that the spatial extent of the hot gas is more than 100 kpc from the joint analysis of *Chandra* absorption spectra with the emission measure from literature, but the results are inconsistent with the Galactic source absorption lines as well as previous studies (Yao & Wang 2007; Yao et al. 2009; Hagihara et al. 2010). Various issues about the data analysis and interpretation of Gupta et al. (2012) were raised by Wang & Yao (2012).

In this paper, we revisit the Mkn 421 direction using the *Suzaku* observed emission spectra to jointly analyze with the absorption spectrum from *Chandra*. Compared to the *Rosat* detector, the *Suzaku* CCD has a better sensitivity and a better energy resolution to separate the hot gaseous disk from the SWCX and LHB ones.

In Section 2, we describe our observations and data-reduction processes. We discuss our data analysis in Section 3, and conclude the discussion in Section 4. Throughout the paper, the statistical errors are quoted at the 90% confidence level in the text, as well as in the tables, while the 68% ( $1\sigma$ ) confidence errors are adopted in the figures, unless otherwise specified.

## 2. Observations and Data Reduction

### 2.1. *Chandra* Observations and Data Reduction

As one of the brightest X-ray sources, Mkn 421 has been observed by *Chandra* many times, using the High-Energy Transmission Grating (HETG) with the Advanced CCD Imaging Spectrometer (ACIS-S) and the Low-Energy Transmission Grating (LETG) with either the ACIS-S or the High-Resolution Camera (HRC-S) aboard. The LETG provides  $\sim 30$ – $40$  cm $^2$  effective area at O VII and O VIII  $K\alpha$  wavelengths with a modest resolution of  $\sim 750$  km s $^{-1}$  (FWHM).

We have used the same absorption spectra as in Yao & Wang (2007), which resulted from combining the six long exposures of the existing observations (Table 1).

### 2.2. *Suzaku* Observations and Data Reduction

We observed the emission from the two off-fields of the Mkn 421 sight line during the AO4 program. The detailed *Suzaku* observation log of the two fields, Obs1 and Obs2, is listed

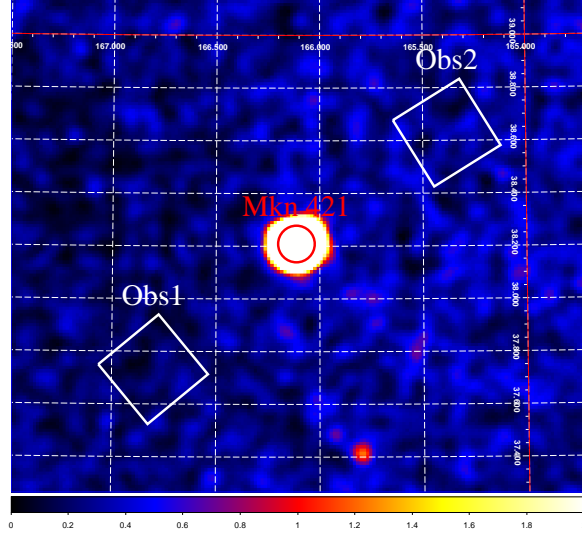


**Fig. 1.** RASS 0.1 - 2.4 keV band X-ray mapping in the vicinity of Mkn 421 (at the center, spread by the *ROSAT* point-spread function) and the XIS FOVs of the two presented observations.

**Table 1.** *Chandra* observation log.

Obs ID	Obs Date	Grating	Detector	Exposure (ks)
4148	2002-10-26	LETG	ACIS	96.84
4149	2003-07-01	LETG	HRC	99.98
5171	2004-07-03	LETG	ACIS	67.15
5318	2004-05-06	LETG	ACIS	30.16
5331	2004-07-12	LETG	ACIS	69.50
5332	2004-07-14	LETG	ACIS	67.06

in Table 2.

We used the CCD camera, the X-ray Imaging Spectrometer (XIS: Koyama et al. 2007), aboard *Suzaku* (Mitsuda et al. 2007) for our observations. To minimize stray light from the Mkn 421, the *Suzaku* XIS fields of view (FOV) of the two observations were chosen to be at least 30' away from the Mkn 421 (Figure 1). The XIS was set to the normal clocking mode and the data format was either  $3 \times 3$  or  $5 \times 5$ . The Spaced-row Charge Injection (SCI) was on for both the observations. Processed data version for the observations is 2.4.12.27. In this work, we used the spectra obtained with XIS 1, which is the backside-illuminated CCD and thus shows superior sensitivity at photon energies below 1 keV comparing to frontside-illuminated CCDs, XIS 0 and XIS 3.

We adopted the same data screening as in Hagihara et al. (2010) to obtain the good time intervals (GTIs), i.e. excluding exposures when the line of sight of *Suzaku* was elevated

**Table 2.** *Suzaku* observation log.

	Obs1	Obs2
$(\alpha, \delta)$ in J2000 ( $^{\circ}$ )	(166.80, 37.73)	(165.38, 38D.63)
$(\ell, b)$ in Galactic coordinate ( $^{\circ}$ )	(180.50, 65.70)	(179.32, 64.36)
Elongation to Mkn 421 ( $^{\circ}$ )	0.76	0.67
Observation ID	504086010	504087010
Observation start time (UT)	2009-11-09T01:34:20	2009-11-11T10:45:08
Observation end time (UT)	2009-11-10T19:25:07	2009-11-13T07:37:24
Exposure time	75 ks	86 ks
Exposure after data reduction	64.3 ks	74.5 ks

above the sunlit limb of Earth by less than  $20^{\circ}$  and exposures with the “cut-off rigidity” less than 8 GV.

### 2.2.1. Contamination from Solar X-rays

The obtained spectra may be contaminated by solar X-rays, scattered off the Earth’s atmosphere into the telescope by either Thompson scattering or fluorescence. As *Suzaku* orbits the Earth with the fixed pointing, the column density of the atmosphere along the line of sight, which depends on the elevation of the satellite, varies rapidly and may affect the intensity of the scattered X-ray intensity. As we are particularly concerned about O VII emission lines around 0.56 keV, we checked the dependency of the 0.4 to 0.7 keV photon counting rate on the Oxygen column density of the sunlit atmosphere in the line of sight using the MSIS atmosphere model (see Fujimoto et al. 2007; Smith et al. 2007; Miller et al. 2008). The result showed no correlation, thus there should be no significant neutral Oxygen emission from the Earth’s atmosphere in the filtered data.

### 2.2.2. Contamination from the Geocoronal SWCX

The obtained spectra may also be contaminated by the SWCX induced emission from the geocorona (Fujimoto et al. 2007). The contamination can be reduced by excluding the exposure time meeting the following three criteria: the excessive solar-wind proton flux, solar-wind ion flux, and the small Earth-to-magnetopause (ETM) distance.

For the solar-wind proton flux and ion flux, we used data obtained with the Solar Wind Electron Proton and Alpha Monitor (SWEPAM), the Solar Wind Ion Composition Spectrometer (SWICS) and the Solar Wind Ion Mass Spectrometer (SWIMS) aboard the *Advanced Composition Explorer (ACE)*, and the Solar Wind Experiment (SWE) aboard the *WIND*. The light curves of XIS-BI in the energy range of 0.5 to 0.7 keV for Obs1 and Obs2, along with their proton flux and ion flux are shown in Figure 2. We could see short time periods when the proton flux in the solar wind exceeded the typical threshold,  $4 \times 10^8 \text{ cm}^{-2} \text{ s}^{-1}$  (Masui et al. 2009), in the beginning of Obs1 observation, however, we did not remove the intervals since the O VIII ion flux stayed far below the typical value reported in Koutroumpa

et al. (2006). Figure 3 shows the spectra of the Obs1 observation for the time intervals in the first half and the last half. Since we could not see a significant discrepancy between the two spectra, the exceeded proton flux should not significantly affect the Obs1 spectrum. For Obs2, we did not remove any time intervals either, since both the proton flux and ion flux are below the threshold throughout the observation.

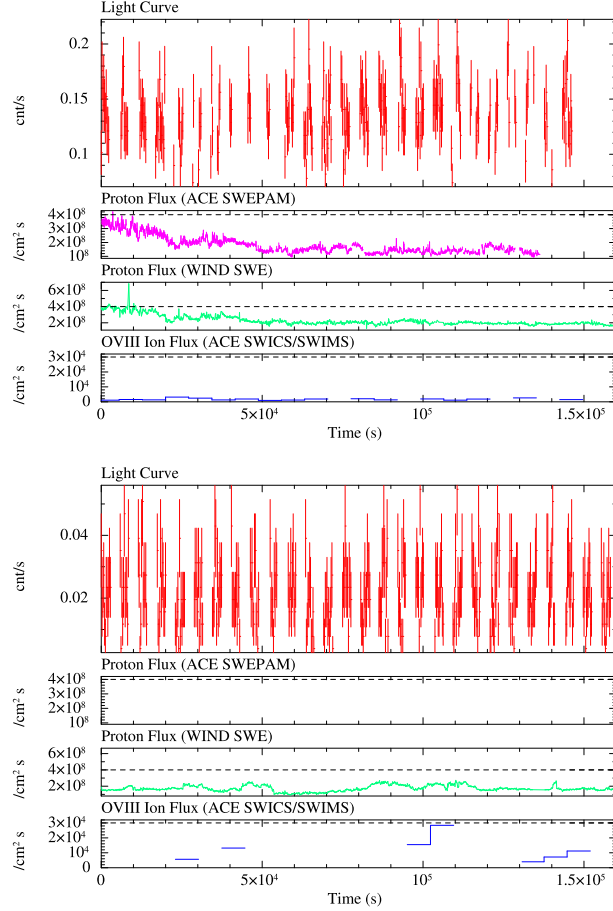


**Fig. 2.** XIS-BI light curve in 0.5–0.7 keV for Obs1 (top panel) and Obs2 (bottom panel), and respective *ACE* SWEPAM (64 sec bin) and *WIND* SWE (90 sec bin) observed proton flux, and *ACE* SWICS/SWIMS (2 hour average) observed O VIII ion flux. The origins of both *ACE* and *WIND* are set to the beginning of the *Suzaku* observations.

The last criteria was the ETM distance in the line sight of *Suzaku* (Fujimoto et al. 2007), which should be  $> 5R_E$  to avoid the contamination. For both Obs1 and Obs2, the ETM distances were more than  $10R_E$  all the time.

### 2.2.3. Point Source Removal

We then constructed an image in the 0.5 to 1.2 keV energy range and detected one point source each in the FOVs of Obs1 and Obs2. We removed circular regions centered at those point sources with the radius of  $2'$  (Figure 4). The radius was determined so that the number of counts from the point sources outside the circular region is less than 3% of that from the

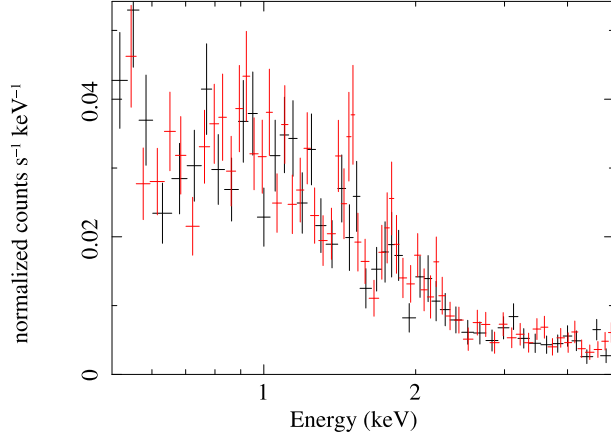


**Fig. 3.** Energy spectra of Obs1 for the time intervals in the first half (black) and the last half (red). There is no significant discrepancy between the two spectra.

diffuse X-ray emission in the energy range.

#### 2.2.4. Considerable stray light from Mkn 421

In both the *Suzaku* observations, we found a discrepancy in the brightness between the near side and the far side of the images toward Mkn 421 (Figure 4). In both images the far side toward Mkn 421 is brighter than the other indicating stray light from Mkn 421 likely caused by the secondary refraction at the X-ray telescope (Serlemitsos et al. 2007; Takei et al. 2012). Figure 5 shows the spectra of the near side and the far side of the images for Obs1 and Obs2. There are large discrepancies between the two spectra in  $< 2.0$  keV for both Obs1 and Obs2. To minimize the confusion caused by the stray light, we used uncontaminated regions for the further analysis. The regions were determined by the following method. We first extracted the images for the 0.5 to 1.2 keV range in the DET coordinates with 8 pixels per bin, then projected the photon count to the DETY axis. Figure 6 shows the result of the projection, along with the best-fitted *constant + linear* given by

$$N_{\gamma} = \begin{cases} b & (DETY < a) \\ c \times (DETY - a) + b & (DETY > a) \end{cases} \quad (1)$$

for Obs1 and

$$N_{\gamma} = \begin{cases} c \times (DETY - a) + b & (DETY < a) \\ b & (DETY > a) \end{cases} \quad (2)$$

for Obs2. The fitted results are shown in Table 3. We first estimated the maximum (minimum for Obs2) error-allowed break-point ( $a$ ), 70.4 bins for Obs1 and 47.9 bins for Obs2, and then calculated the DETY length of the region to maximize the size of the retained regions (dashed green boxes in Figure 4) for better statistics of the extracted emission spectra.



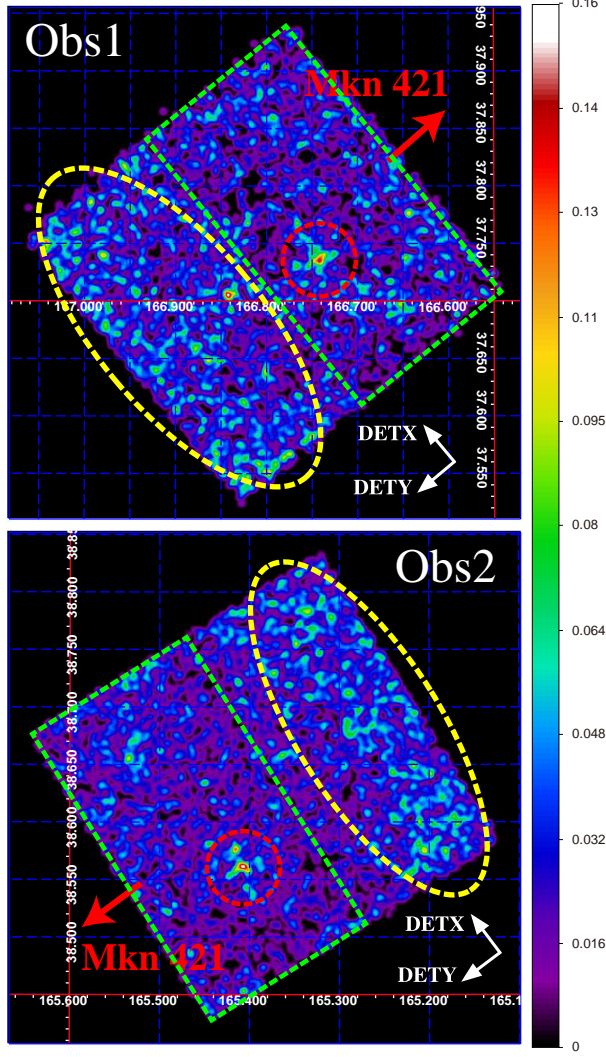


**Fig. 4.** 0.5–1.2 keV XIS-BI images of Obs1 (top) and Obs2 (bottom). Point sources were removed with the radius of  $2'$  (dashed red circle). On the opposite sides of Mkn 421 (red allow) the diffuse emission is enhanced in both observations (dashed yellow circle), which are considered to be due to stray light from Mkn 421. The regions were carefully chosen to minimize the contamination from the stray light (dashed green box).

**Table 3.** Fitting results of the DETY projected photon counts in the energy range from 0.5 to 1.2 keV with *constant* + *linear* for both Obs1 and Obs2 ( $1\sigma$  confidence level).

	Break (a)	Const (b)	Slope (c)	$\chi^2/\text{dof}$
	(bin)*	(bin)*	(bin)*	
Obs1	$65.0 \pm 5.4$	$25.4 \pm 0.6$	$0.29 \pm 0.04$	165.3/125
Obs2	$51.1 \pm 3.2$	$34.2 \pm 0.7$	$-0.57 \pm 0.06$	151.8/125

\* 8 pixels per bin.



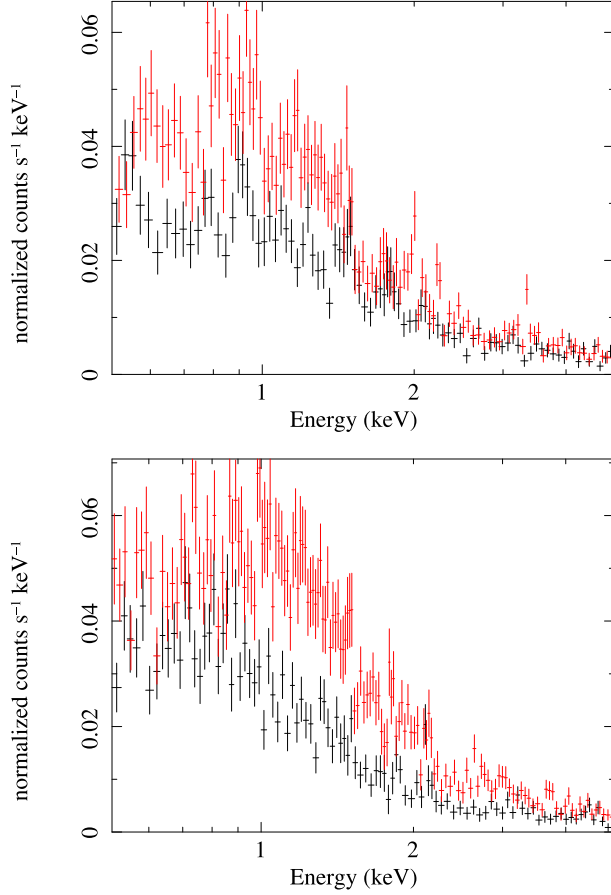


**Fig. 5.** Energy spectra of the regions, the near side (black) and the far side (red) toward Mkn 421, for Obs1 (top) and Obs2 (bottom).

### 2.2.5. Background and response

ARFs used in this work for *Suzaku* observed spectra were generated using `xissimarfgen`, in which source mode is set to UNIFORM with the radius of 20' to take diffuse stray light effects into account. We then used `marfmr` to combine ARFs with RMFs, which were generated using `xisrmfgen`, to generate response files. Non-X-ray backgrounds were generated using `xisnxbgen` as described in Tawa et al. (2008).

## 3. Spectral Analysis and Results

The spectral analysis was performed using XSPEC v12.7.1. We adopted the solar abundances as given in Anders & Grevesse (1989).

### 3.1. Chandra X-Ray Absorption Spectrum

We first measured the equivalent widths (EWs) of the absorption lines of the highly ionized oxygen ions, which we have a great interest in. We therefore fitted the *Chandra*-observed Mkn 421 spectrum only for the energy range of 0.55 to 0.68 keV using a model, Abs(a), that

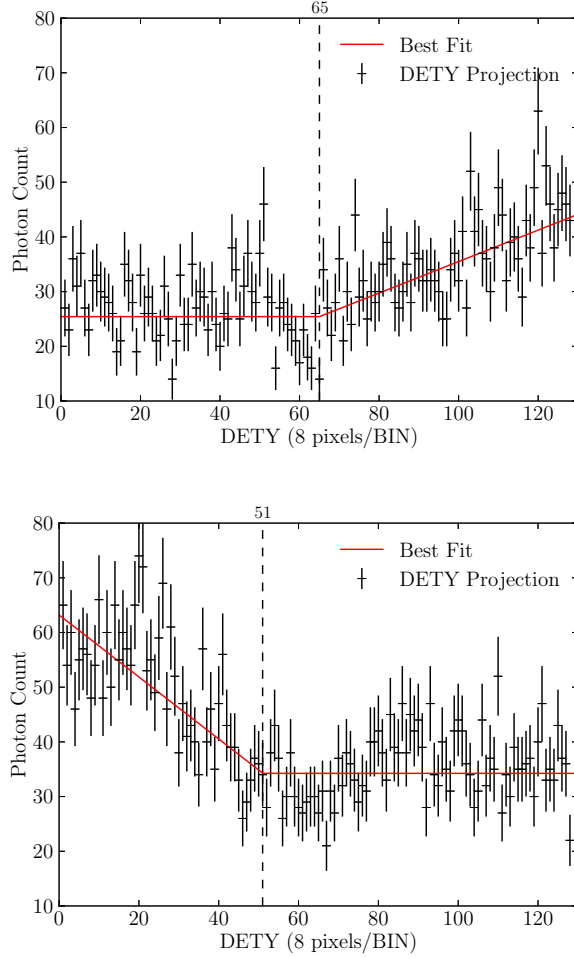


**Fig. 6.** DEITY projected 0.5–1.2 keV photon counts and the best-fitted *constant* + *linear* for Obs1 (Top) and Obs2 (Bottom).

consists of a *power-law* and three *gaussian* functions convolved with absorption by the neutral ISM (*wabs*: Morrison & McCammon 1983), then obtained the centroids, sigmas and equivalent widths of O VII  $K\alpha$ , O VIII  $Ly\alpha$  and O VII  $K\beta$  absorption lines as shown in Figure 7. In the fitting, we ignored the energy range of 0.63 to 0.65 keV (the residuals in this range are plotted in Figure 7 in red) due to artificial features (likely caused by the iodine M-edge of HRC) seen in the spectrum that significantly worsen the goodness of fit. The column density of neutral hydrogen was fixed to  $1.92 \times 10^{20}$  atoms  $\text{cm}^{-2}$  determined by the LAB Survey of Galactic H I in this direction (Kalberla et al. 2005). The fit results are shown in Table 4. The measured EWs were consistent with those reported by Williams et al. (2005).

We then replaced the *gaussian* functions by *absem* functions. The *absem*, which is a revision of the *absline* function of Yao & Wang (2005), can be used to jointly fit the absorption and the emission spectra (see Yao & Wang 2007 and Yao et al. 2009 for a detailed description).

Assuming a gas with a uniform density and a single temperature, we first performed a

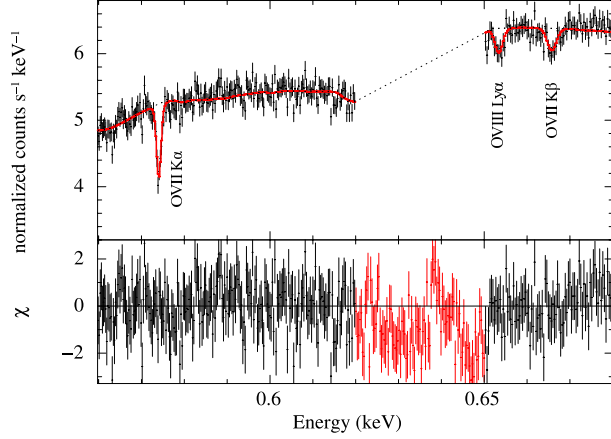


**Fig. 7.** *Chandra* spectrum of Mkn 421 for the 0.55–0.7 keV range, fitted with the *wabs(power-law + 3 × Gaussian)* model. The energy range of 0.63 to 0.65 keV was ignored due to artificial features seen in the spectrum, but the residuals in this range are plotted in red.

**Table 4.** Spectral fitting of absorption data with *wabs(power-law + 3 × Gaussian)* model.

	O VII K $\alpha$	O VIII Ly $\alpha$	O VII K $\beta$
Centroid (eV)	$574.0^{+0.1}_{-0.1}$	$653.4^{+0.4}_{-0.3}$	$665.8^{+0.4}_{-0.4}$
Sigma (eV)	$0.18^{+0.14}_{-0.18}$	$0.65^{+0.54}_{-0.39}$	$0.84^{+0.68}_{-0.56}$
EW (eV)	$0.295^{+0.022}_{-0.024}$	$0.138^{+0.028}_{-0.031}$	$0.145^{+0.033}_{-0.034}$

joint analysis of O VII K $\alpha$  and O VII K $\beta$  to constrain the O VII column density and the velocity dispersion  $v_b$ . With the constrained  $v_b$ , adding the O VIII K $\alpha$  line in the analysis also yields the column density of O VIII. We call this model as Abs(b). Since the ratio of column densities of O VII and O VIII is sensitive to the gas temperature, a joint analysis named Abs(c) of the O VII and O VIII lines constrains the gas temperature. Assuming the solar abundance for oxygen, and given the constrained gas temperature, the O VII (or O VIII) column density can be converted to the corresponding hot-phase hydrogen column density. This final model is Abs(d). The results of each steps are listed in Table 5. The constrained O VII column density,  $(8.1^{+3.9}_{-3.1}) \times 10^{15} \text{ cm}^{-2}$ , is comparable to typical values  $\sim 10^{16} \text{ cm}^{-2}$  obtained from AGN observations given in two systematic studies (Fang et al. 2006; Bregman & Lloyd-Davies 2007).

### 3.2. *Suzaku* X-Ray Emission Spectra

We first individually fitted the two *Suzaku* emission spectra extracted for the background emission in the Mkn 421 field. The model function of the fits consists of an absorbed *power-law* for the CXB, an absorbed *Mekal* for the hot ISM, and an unabsorbed *Mekal* for the SWCX and LHB contributions. The temperature and normalization of the SWCX and LHB component are fixed initially so that it produces a 2.0 LU O VII line intensity, which is a typical intensity from Heliospheric SWCX and LHB (Yoshino et al. 2009). The systematic error of this step is

**Table 5.** Spectral fitting result of absorption data with  $wabs(power-law) \times absem \times absem \times absem$  model.

	Galactic	Hot ISM					$\chi^2/\text{dof}$
	$\Gamma$	$v_b$ (km s $^{-1}$ )	$\log T$ (K)	$\log N_{\text{OVII}}$ (cm $^{-2}$ )	$\log N_{\text{OVIII}}$ (cm $^{-2}$ )	$\log N_{\text{H}}$ (cm $^{-2}$ )	
Abs(b)	$2.24^{+0.04}_{-0.04}$	$60^{+45}_{-13}$	...	$15.98^{+0.17}_{-0.20}$	$15.22^{+0.14}_{-0.16}$	...	284.81/294
Abs(c)	$2.24^{+0.04}_{-0.04}$	$62^{+43}_{-16}$	$6.18^{+0.03}_{-0.04}$	$15.96^{+0.19}_{-0.17}$	...	...	284.84/294
Abs(d)	$2.24^{+0.04}_{-0.04}$	$60^{+45}_{-14}$	$6.17^{+0.03}_{-0.03}$	...	...	$19.13^{+0.16}_{-0.18}$	284.81/294

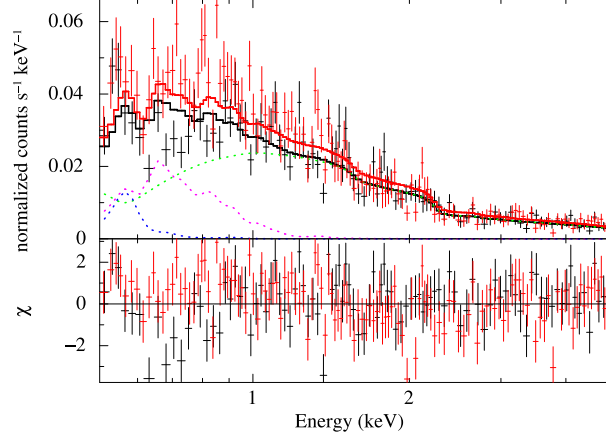


**Fig. 8.** *Suzaku* spectrum of Obs1 (black) and Obs2 (red), and the best-fitted model convolved with the instrument response function. The residuals of the fit are shown in the lower panel. The model function, denoted as Emission(A), consists of three spectral components; a *power-law* for the CXB (green), a *Mekal* for the hot ISM (magenta), and another *Mekal* for the SWCX+LHB (blue). The components of Obs2 are intentionally omitted in the figure for clarity.

discussed in Section 4.2. The fitted results are shown in Table 6 as Obs1 and Obs2(a). We then jointly fitted the Obs1 and Obs2 spectra with the same model (Figure 8); all parameters, except for the normalizations of the CXB component, were linked between the Obs1 and Obs2. The results are shown in the same table as Emission(A).

The  $\chi^2$  of this joint fit is worse than those of fits to the Obs1 and Obs2 spectra, individually, apparently due to the excess seen in the Obs2 spectrum in the energy range from 0.6 to 1.0 keV. Similar excesses have been seen in the *Suzaku* spectra of the diffuse emission. Yoshino et al. (2009) reported that the excess can be explained by either over abundances of some metal elements or an additional higher temperature emission component with solar abundances. The latter explanation is considered to be plausible due to the putative presence of blobs of high ( $> 0.22$  keV) temperature hot gas in the fields (Yoshino et al. 2009).

So we carried out additional fits for Obs2; a fit with an absorbed *power-law* for the CXB, an absorbed *Mekal* for the hot ISM, of which Ne and Fe abundances were allowed to vary, and an unabsorbed *Mekal* for the SWCX and LHB (Figure 9), and a fit with an absorbed *power-law*

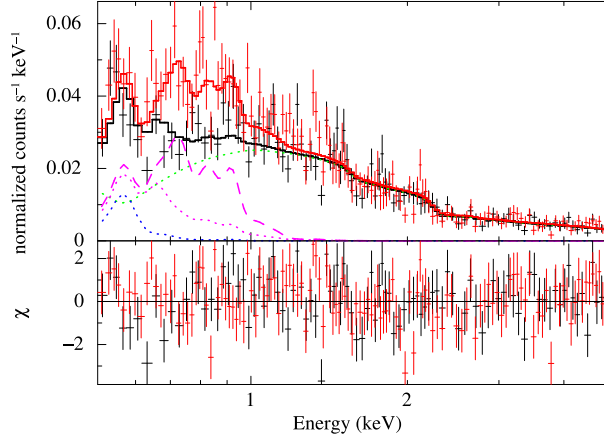


**Fig. 9.** *Suzaku* spectrum of Obs1 (black) and Obs2 (red), and the best-fitted model and its components. The model function, denoted as Emission(B), consists of three spectral components; a *power-law* for the CXB (green), a *Mekal* for the hot ISM (dotted-magenta for Obs1 and dashed-magenta for Obs2), and another *Mekal* for the SWCX+LHB (blue). For Obs2, the hot-ISM component is only shown in the figure for clarity.

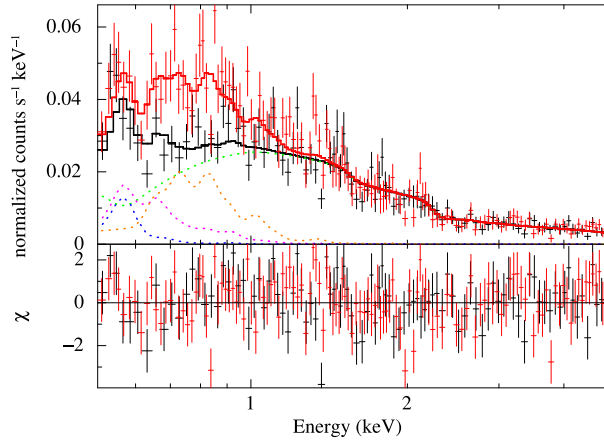


**Fig. 10.** *Suzaku* spectrum of Obs1 (black) and Obs2 (red), and the best-fitted model and its components. The model function consists of four spectral components; a *power-law* for the CXB (green), a *Mekal* for the hot ISM (magenta), a *Mekal* for the SWCX+LHB (blue), and a *Mekal* for a LTC emission (orange). The components of Obs2 except the LTC emission are intentionally omitted in the figure for clarity.

for the CXB, an absorbed *Mekal* for the hot ISM, an unabsorbed *Mekal* for the SWCX and LHB, and one more *Mekal* for a local thermal component (hereafter LTC) (Figure 10). The fitted results of those three are listed in Table 6 as Obs2(b) and Obs2(c), respectively. The  $\chi^2$  values were then improved in both fits, however, the temperature of hot ISM for Obs2(b) is still slightly higher than that of Obs1 while that of Obs2(c) is almost comparable. We then combined them with the Obs1 spectrum. The results are listed in the same table as Emission(B) and Emission(C) that correspond to joint fits of Obs1 with Obs2(b) and Obs2(c) respectively. In both fits, the  $\chi^2$  values were also improved compared with that of Emission(a).

**Table 6.** Spectral fitting results of the emission data.

	CXB	LHB+SWCX		Hot ISM				LTC		$\chi^2/\text{dof}$
	Norm <sup>†</sup>	log $T$ (K)	Norm <sup>‡</sup>	log $T$ (K)	Norm <sup>‡</sup>	Ne/O	Fe/O	log $T$ (K)	Norm <sup>‡</sup>	
Obs1	$12.2^{+0.5}_{-0.5}$	6.06 (fix)	6.6 (fix)	$6.35^{+0.07}_{-0.05}$	$2.1^{+0.6}_{-0.6}$	1 (fix)	1 (fix)	...	...	123.77/99
Obs2(a)	$10.9^{+0.5}_{-0.5}$	6.06 (fix)	6.6 (fix)	$6.46^{+0.03}_{-0.03}$	$3.1^{+0.4}_{-0.4}$	1 (fix)	1 (fix)	...	...	144.44/126
Obs2(b)	$10.8^{+0.5}_{-0.5}$	6.06 (fix)	6.6 (fix)	$6.44^{+0.06}_{-0.10}$	$3.0^{+0.5}_{-0.5}$	$2.1^{+2.6}_{-1.0}$	$1.2^{+2.6}_{-0.6}$	...	...	140.90/124
Obs2(c)	$10.6^{+0.5}_{-0.5}$	6.06 (fix)	6.6 (fix)	$6.37^{+0.07}_{-0.07}$	$3.1^{+0.6}_{-0.6}$	1 (fix)	1 (fix)	$6.83^{+0.11}_{-0.30}$	$0.7^{+0.4}_{-0.4}$	135.25/124
Emission(A)										313.32/225
Obs1	$11.4^{+0.5}_{-0.5}$	6.06 (fix)	6.6 (fix)	$6.44^{+0.03}_{-0.02}$	$2.4^{+0.3}_{-0.3}$	1 (fix)	1 (fix)	...	...	
Obs2(a)	$11.5^{+0.4}_{-0.4}$	↑	↑	↑	↑	↑	↑	...	...	
Emission(B)										271.83/223
Obs1	$12.0^{+0.5}_{-0.5}$	6.06 (fix)	6.6 (fix)	$6.35^{+0.04}_{-0.03}$	$2.6^{+0.4}_{-0.4}$	1 (fix)	1 (fix)	...	...	
Obs2(b)	$11.0^{+0.5}_{-0.5}$	↑	↑	↑	↑	$4.8^{+2.3}_{-1.7}$	$4.2^{+3.0}_{-1.4}$	...	...	
Emission(C)										261.00/223
Obs1	$12.2^{+0.5}_{-0.5}$	6.06 (fix)	6.6 (fix)	$6.33^{+0.04}_{-0.06}$	$2.2^{+0.6}_{-0.5}$	1 (fix)	1 (fix)	...	...	
Obs2(c)	$10.8^{+0.5}_{-0.5}$	↑	↑	↑	↑	↑	↑	$6.59^{+0.22}_{-0.07}$	$1.4^{+0.5}_{-0.6}$	

<sup>†</sup> In units of photons keV<sup>-1</sup> cm<sup>-2</sup> s<sup>-1</sup> str<sup>-1</sup> @1keV.

<sup>‡</sup> In units of 10<sup>-3</sup> pccm<sup>-6</sup>. The emission measure of LHB+SWCX is fixed to 0.0066 pccm<sup>-6</sup> which corresponds to 2.0 LU of O VII K $\alpha$  emission.

Finally we reset the oxygen abundance of the *Mekal* components that represent the SWCX/LHB and hot ISM to zero, and added two delta functions at 0.574 keV and 0.654 keV to evaluate the line intensities of the O VII and O VIII emissions. Results are shown in Table 7.

By comparing the obtained line intensities of O VII and O VIII for Obs1 and Obs2 individual fits to their joint fits, we could see that O VII and O VIII line intensities from Emission(C) are consistent with that from the Obs1 individual fit. For the further analysis, we shall therefore employ the model used in Emission(C).

### 3.3. Combined Analysis

If we assume that the hot ISM observed with *Chandra* and the hot ISM observed with *Suzaku* originate from the same hot gas, i.e., the hot ISM is uniform across the angular extent of the observed fields, the column density of absorption spectrum and the emission measure of emission spectra linked with common parameters should estimate the plasma scale and temperature.

If the ISM were an isothermal plasma with a uniform density in the solar abundance, the column density of hydrogen ( $CD$ ) and the emission measure ( $EM$ ) are then given as

$$CD = nL \quad (3)$$

$$EM = (1 + 2A_{\text{He}})n^2L \quad (4)$$

**Table 7.** O VII and O VIII line intensities.

	CXB	Hot ISM		LTC		O VII	O VIII	Flux <sup>  </sup>	$\chi^2/\text{dof}$
	Norm <sup>†</sup>	log $T$ (K)	Norm <sup>‡</sup>	log $T$ (K)	Norm <sup>‡</sup>	SB <sup>§</sup>	SB <sup>§</sup>		
Obs1	$12.0^{+0.5}_{-0.5}$	6.35 (fix)	$4.8^{+1.5}_{-1.5}$	...	...	$4.8^{+1.1}_{-1.1}$	$0.6(< 1.1)$	2.38	118.99/96
Obs2(a)	$10.9^{+0.5}_{-0.5}$	6.46 (fix)	$4.0^{+0.5}_{-0.5}$	...	...	$5.8^{+1.0}_{-1.0}$	$2.0^{+0.6}_{-0.6}$	2.86	144.48/125
Obs2(b)	$10.8^{+0.5}_{-0.5}$	6.44 (fix)	$3.6^{+0.5}_{-0.5}$	...	...	$5.8^{+1.0}_{-1.0}$	$2.0^{+0.6}_{-0.6}$	2.85	145.60/125
Obs2(c)	$10.7^{+0.5}_{-0.5}$	6.37 (fix)	$6.2^{+2.8}_{-2.8}$	6.83 (fix)	$0.4^{+0.4}_{-0.4}$	$5.5^{+1.1}_{-1.1}$	$1.9^{+0.6}_{-0.6}$	2.88	140.26/123
Emission(A)									310.37/224
Obs1	$11.3^{+0.5}_{-0.5}$	6.44 (fix)	$3.2^{+0.4}_{-0.4}$	...	...	$5.4^{+0.8}_{-0.8}$	$1.3^{+0.4}_{-0.4}$	2.60	
Obs2(a)	$11.4^{+0.4}_{-0.4}$	↑	↑	...	...	↑	↑	2.60	
Emission(B)									284.38/224
Obs1	$12.1^{+0.5}_{-0.5}$	6.35 (fix)	$3.0^{+0.4}_{-0.4}$	...	...	$5.5^{+0.8}_{-0.8}$	$1.3^{+0.4}_{-0.4}$	2.40	
Obs2(b)	$11.0^{+0.5}_{-0.4}$	↑	↑	...	...	↑	↑	2.74	
Emission(C)									261.07/223
Obs1	$12.0^{+0.5}_{-0.5}$	6.33 (fix)	$5.6^{+1.6}_{-1.6}$	...	...	$4.9^{+0.8}_{-0.8}$	$0.8^{+0.4}_{-0.4}$	2.42	
Obs2(c)	$10.7^{+0.5}_{-0.5}$	↑	↑	6.59 (fix)	$1.2^{+0.3}_{-0.3}$	↑	↑	2.85	

<sup>†</sup> In units of  $\text{photons keV}^{-1} \text{cm}^{-2} \text{s}^{-1} \text{str}^{-1}$  @ 1 keV.

<sup>‡</sup> In units of  $10^{-3} \text{pccm}^{-6}$ .

<sup>§</sup> The surface brightness in units of  $\text{LU} = \text{photons cm}^{-2} \text{s}^{-1} \text{str}^{-1}$ .

<sup>||</sup> 0.5–1.2 keV range, in units of  $10^{-12} \text{erg cm}^{-2} \text{s}^{-1}$ .

where  $n$  is the hydrogen number density,  $A_{\text{He}}$  is the abundance ratio of He to H, and  $L$  is the extent of the plasma along the line of sight. Once  $CD$  and  $EM$  are determined from observations, we can derive  $n_{\text{H}}$  and  $L$  individually.

However, the temperature of the hot ISM obtained from the emission analysis is higher than that obtained from the absorption analysis. To account for the difference, Yao et al. (2009) introduced an exponential disk model. In this model, we assume that the hydrogen number density and temperature can be expressed as

$$n = n_0 e^{-z/(h_n \xi)} \quad \text{and} \quad T = T_0 e^{-z/(h_T \xi)} \quad (5)$$

where  $z$  is the vertical distance from the Galactic plane,  $n_0$  and  $T_0$  are the density and temperature at the plane,  $h_n$  and  $h_T$  are the scale heights of density and temperature, and  $\xi$  is the volume filling factor, which is assumed to be 1 in this work.

We can now corollary derive

$$n = n_0 (T/T_0)^\gamma \quad (6)$$

where  $\gamma \equiv h_T/h_n$ . The differential hydrogen column density distribution can then be deduced as

$$dN_{\text{H}} = n dL = \frac{N_{\text{H}} \gamma}{T_0} \left( \frac{T}{T_0} \right)^{\gamma-1} dT. \quad (7)$$



Meanwhile, the line intensity  $I$  can be expressed as

$$I = \frac{1}{4\pi} \int_{T_{\min}}^{T_0} \Lambda(T) \frac{dEM}{dT} dT, \quad (8)$$

where  $\Lambda(T)$  is the emissivity of the hot gas, and the differential EM is

$$dEM = n_e n_H dL = \frac{1.2 N_H^2 \gamma}{T_0 L} \left( \frac{T}{T_0} \right)^{2\gamma-1} dT, \quad (9)$$

where  $L = h_n \xi / \sin b$ .

To perform a joint analysis using the *Chandra* absorption spectrum and the *Suzaku* emission spectra, we first replaced the *Mekal* functions used in the emission analysis by *vabmkl* functions (Yao et al. 2009) that directly take  $T_0$ ,  $N_H$  and  $L$  as parameters and calculate an emission measure internally. We then linked the  $T_0$  and  $N_H$  parameters to those of the *absem* components used in the absorption analysis.

We performed three fits using the best-fitted, lower- and upper-limit LTC temperatures. In these fits,  $h_n$  tended to be infinity while  $\gamma$  tended to be zero, indicating that the density stays almost uniform while the temperature drops exponentially away from the plane. For this reason, we changed the parameters  $h_n$  and  $N_H$  of *vabmkl* to  $h_T$  and  $\gamma N_H$  respectively. The fitted results are shown in Table 8. We obtained the scale heights for the temperature and density as  $h_T = 1.6_{-0.7}^{+1.7}$  kpc and  $h_n > 2.8$  kpc and the density at the plane as  $n_0 = (1.2_{-0.4}^{+0.5}) \times 10^{-3} \text{ cm}^{-3}$ . Confidence contours of  $h_T$ ,  $T_0$  and  $\gamma N_H$  versus  $\gamma$ , and  $\gamma N_H$  versus  $h_T$  are shown in Figure 11 and Figure 12, respectively.

Finally, we fixed  $\gamma$  to 1 or 1.5 for the scale height ratio of density and temperature of an ideal gas. The results are also shown in the same table.

## 4. Discussion

### 4.1. Excess in Obs2 spectrum

There was a large discrepancy in the spectra extracted from Obs1 and Obs2. The spectrum of Obs2 shows the excess in the energy range from 0.6 to 1.0 keV. Yoshino et al. (2009) observed twelve blank fields with *Suzaku* and found similar excesses in four of them. As the excesses, seen in one third of the observations, are not extraordinary. The excess seen Obs2 may be rare because it is just a degree away from Obs1. Yao et al. (2009), Hagihara et al. (2010) and this paper assumed that emissions from two *Suzaku* observations  $1^\circ$  apart on the opposite sides of the respective X-ray sources are the same. But this may be too simplistic. To estimate the effect of the fluctuation, we jointly fitted the absorption spectrum with each emission spectra. The results in Table 9 indicate that this degree of fluctuation does not affect the characteristic of the hot ISM, as inferred from our analysis.

What could be the cause of such fluctuation? The temperature of the excess seems too high to be a fluctuation in the LHB. It may be due to the cosmic variance (extragalactic

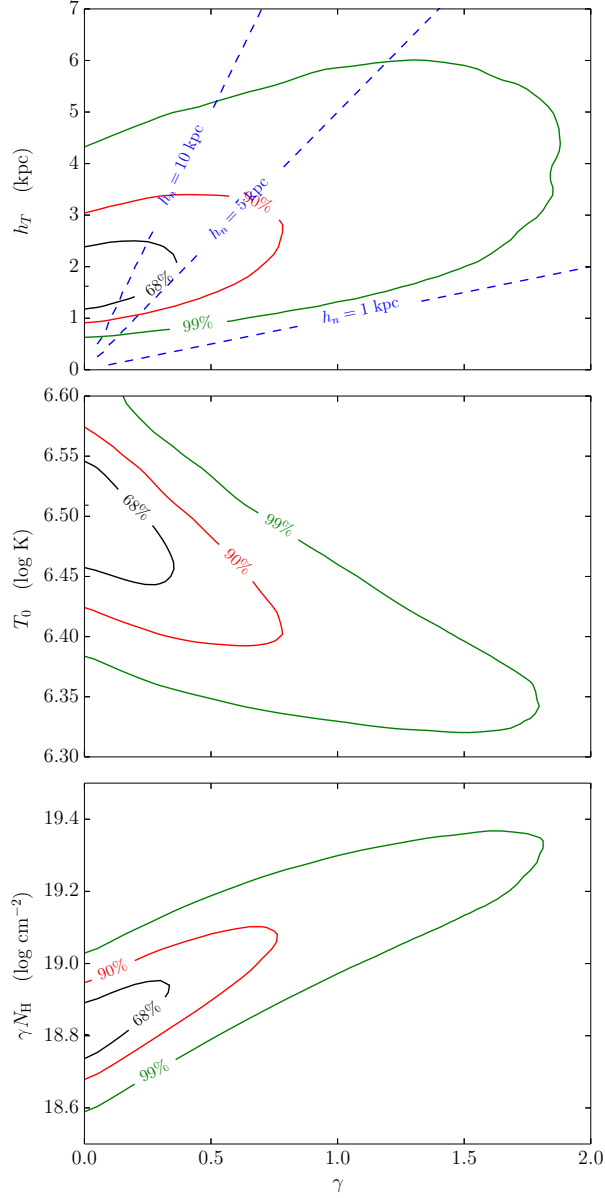


**Fig. 11.** 68%, 90% and 99% confidence contours of  $h_T$ ,  $T_0$  and  $N_H$  vs.  $\gamma$ , obtained from joint fits to the X-ray absorption and emission data adopting the exponential model.  $v_b$  is thawed freely during fits, and the surface brightness of LHB+SWCX is fixed to 2 LU. The temperature and emission measure of the LTC are fixed to the best-fitted values of the emission analysis. In top panel, the scale height of the density ( $h_n$ ) is constant along the dashed lines.

**Table 8.** Spectral fitting results in the Exponential model.

CXB		Hot ISM					LTC		$\chi^2/\text{dof}$
	Norm <sup>†</sup>	$v_b$	$\log T_0$	$\log(\gamma N_{\text{H}})$	$h_T$	$\gamma$	$\log T$	Norm <sup>‡</sup>	
		(km s <sup>-1</sup> )	(K)	(cm <sup>-2</sup> )	(kpc)		(K)		
LHB+SWCX = 2 LU <sup>§</sup>									
Exp(C)									543.52/518
Abs	...	59 <sup>+31</sup> <sub>-12</sub>	6.51 <sup>+0.07</sup> <sub>-0.12</sub>	18.80 <sup>+0.31</sup> <sub>-0.14</sub>	1.6 <sup>+1.7</sup> <sub>-0.7</sub>	0.00(< 0.74)	...	...	
Obs1	12.1 <sup>+0.5</sup> <sub>-0.5</sub>	...	↑	↑	↑	↑	...	...	
Obs2(c)	10.8 <sup>+0.5</sup> <sub>-0.5</sub>	...	↑	↑	↑	↑	6.59 (fix)	1.3 <sup>+0.3</sup> <sub>-0.3</sub>	
Exp(C); LTC Lower Limit									544.53/518
Abs	...	61 <sup>+30</sup> <sub>-13</sub>	6.55 <sup>+0.07</sup> <sub>-0.08</sub>	18.79 <sup>+0.22</sup> <sub>-0.14</sub>	1.9 <sup>+1.6</sup> <sub>-0.9</sub>	0.00(< 0.46)	...	...	
Obs1	12.0 <sup>+0.5</sup> <sub>-0.5</sub>	...	↑	↑	↑	↑	...	...	
Obs2(c)	10.8 <sup>+0.5</sup> <sub>-0.5</sub>	...	↑	↑	↑	↑	6.52 (fix)	1.5 <sup>+0.4</sup> <sub>-0.4</sub>	
Exp(C); LTC Upper Limit									547.14/518
Abs	...	59 <sup>+38</sup> <sub>-9</sub>	6.50 <sup>+0.07</sup> <sub>-0.10</sub>	18.80 <sup>+0.18</sup> <sub>-0.13</sub>	1.4 <sup>+1.6</sup> <sub>-0.6</sub>	0.00(< 0.77)	...	...	
Obs1	11.9 <sup>+0.5</sup> <sub>-0.5</sub>	...	↑	↑	↑	↑	...	...	
Obs2(c)	10.6 <sup>+0.5</sup> <sub>-0.5</sub>	...	↑	↑	↑	↑	6.81 (fix)	0.8 <sup>+0.2</sup> <sub>-0.2</sub>	
Exp(C); Fixed $\gamma$									547.63/519
Abs	...	79 <sup>+36</sup> <sub>-13</sub>	6.39 <sup>+0.07</sup> <sub>-0.06</sub>	19.08 <sup>+0.04</sup> <sub>-0.04</sub>	2.2 <sup>+0.8</sup> <sub>-0.4</sub>	1.0 (fix)	...	...	
Obs1	12.3 <sup>+0.4</sup> <sub>-0.5</sub>	...	↑	↑	↑	↑	...	...	
Obs2(c)	10.8 <sup>+0.4</sup> <sub>-0.5</sub>	...	↑	↑	↑	↑	6.59 (fix)	1.5 <sup>+0.2</sup> <sub>-0.3</sub>	
Exp(C); Fixed $\gamma$									548.65/519
Abs	...	77 <sup>+200</sup> <sub>-26</sub>	6.36 <sup>+0.05</sup> <sub>-0.06</sub>	19.25 <sup>+0.17</sup> <sub>-0.19</sub>	3.5 <sup>+3.5</sup> <sub>-1.9</sub>	1.5 (fix)	...	...	
Obs1	12.3 <sup>+0.5</sup> <sub>-0.5</sub>	...	↑	↑	↑	↑	...	...	
Obs2(c)	10.7 <sup>+0.4</sup> <sub>-0.5</sub>	...	↑	↑	↑	↑	6.59 (fix)	1.5 <sup>+0.3</sup> <sub>-0.2</sub>	

<sup>†</sup> In units of photons keV<sup>-1</sup> cm<sup>-2</sup> s<sup>-1</sup> str<sup>-1</sup> @1keV.

<sup>‡</sup> In units of 10<sup>-3</sup> pccm<sup>-6</sup>.

<sup>§</sup> Emission measure of *mekal* for LHB+SWCX is set to 0.0066 pccm<sup>-6</sup>, which corresponds to 2.0 LU O VII K $\alpha$  emission.

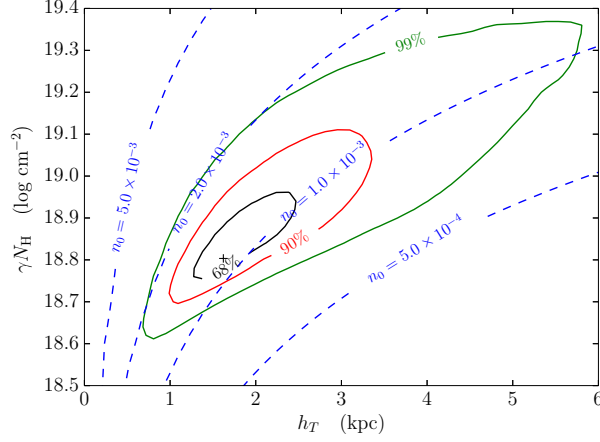


**Fig. 12.** 68%, 90% and 99% confidence contours of  $h_T$  vs.  $N_H$ , obtained from joint fits to the X-ray absorption and emission data adopting the exponential model.  $v_b$  is thawed freely during fits, and the surface brightness of LHB+SWCX is fixed to 2 LU. The temperature and emission measure of the LTC are fixed to the best-fitted values of the emission analysis. The density at the Galactic plane  $n_0$  is constant along the dashed lines.

**Table 9.** Spectral fitting results in the Exponential model fitting the absorption and the emissions with each.

	CXB		Hot ISM				LTC		$\chi^2/\text{dof}$
	Norm <sup>†</sup>								
		$v_b$ (km s <sup>-1</sup> )	$\log T_0$ (K)	$\log(\gamma N_{\text{H}})$ (cm <sup>-2</sup> )	$h_T$ (kpc)	$\gamma$	$\log T$ (K)	Norm <sup>‡</sup>	
LHB+SWCX = 2 LU <sup>§</sup>									
With Obs1									412.65/391
Abs	...	45 <sup>+14</sup> <sub>-9</sub>	6.42 <sup>+0.14</sup> <sub>-0.16</sub>	19.10 <sup>+0.48</sup> <sub>-0.23</sub>	4.7 <sup>+3.7</sup> <sub>-2.6</sub>	0.00(< 3.25)	...	...	
Obs1	12.3 <sup>+0.6</sup> <sub>-0.5</sub>	...	↑	↑	↑	↑	...	...	
With Obs2(a)									423.9/420
Abs	...	65 <sup>+31</sup> <sub>-15</sub>	6.69 <sup>+0.05</sup> <sub>-0.07</sub>	18.74 <sup>+0.16</sup> <sub>-0.14</sub>	1.2 <sup>+1.2</sup> <sub>-0.6</sub>	0.00(< 0.14)	...	...	
Obs2(a)	10.7 <sup>+0.5</sup> <sub>-0.5</sub>	...	↑	↑	↑	↑	...	...	
With Obs2(b)									421.60/420
Abs	...	63 <sup>+17</sup> <sub>-10</sub>	6.62 <sup>+0.06</sup> <sub>-0.05</sub>	18.76 <sup>+0.13</sup> <sub>-0.05</sub>	1.1 <sup>+0.5</sup> <sub>-0.2</sub>	0.00(< 0.32)	...	...	
Obs2(b) <sup>  </sup>	10.7 <sup>+0.5</sup> <sub>-0.5</sub>	...	↑	↑	↑	↑	...	...	
With Obs2(c)									420.08/419
Abs	...	61 <sup>+48</sup> <sub>-9</sub>	6.56 <sup>+0.13</sup> <sub>-0.13</sub>	18.78 <sup>+0.26</sup> <sub>-0.13</sub>	1.1 <sup>+1.1</sup> <sub>-0.5</sub>	0.00(< 0.67)	...	...	
Obs2(c)	10.6 <sup>+0.5</sup> <sub>-0.5</sub>	...	↑	↑	↑	↑	6.83 (fix)	0.5 <sup>+0.4</sup> <sub>-0.5</sub>	

<sup>†</sup> In units of photons keV<sup>-1</sup> cm<sup>-2</sup> s<sup>-1</sup> str<sup>-1</sup> @1keV.

<sup>‡</sup> In units of 10<sup>-3</sup> pccm<sup>-6</sup>.

<sup>§</sup> Emission measure of *mekal* for LHB+SWCX is set to 0.0033 pccm<sup>-6</sup>, which corresponds to 1.0 LU O VII K $\alpha$  emission as the estimated lower limit.

<sup>||</sup> Abundances of Ne and Fe are set to 2.1 and 1.2 respectively, according to the Obs2(c) fit in Table 6.

**Table 10.** Spectral fitting results of emission data using the lower and upper limits of SWCX and LHB.

	CXB	LHB+SWCX		Hot ISM				LTC		$\chi^2/\text{dof}$
	Norm <sup>†</sup>	log $T$ (K)	Norm <sup>‡</sup>	log $T$ (K)	Norm <sup>‡</sup>	Ne/O	Fe/O	log $T$ (K)	Norm <sup>‡</sup>	
LHB+SWCX = 1 LU <sup>§</sup> (Lower Limit)										
Emission(C)										262.89/223
Obs1	12.2 <sup>+0.5</sup> <sub>-0.5</sub>	6.06 (fix)	3.3 (fix)	6.31 <sup>+0.02</sup> <sub>-0.06</sub>	3.2 <sup>+0.7</sup> <sub>-0.4</sub>	1 (fix)	1 (fix)	...	...	
Obs2(c)	10.7 <sup>+0.5</sup> <sub>-0.5</sub>	↑	↑	↑	↑	↑	↑	6.63 <sup>+0.18</sup> <sub>-0.10</sub>	1.3 <sup>+0.2</sup> <sub>-0.4</sub>	
LHB+SWCX = 3 LU <sup>  </sup> (Upper Limit)										
Emission(C)										259.21/223
Obs1	12.1 <sup>+0.6</sup> <sub>-0.5</sub>	6.06 (fix)	9.8 (fix)	6.43 <sup>+0.10</sup> <sub>-0.10</sub>	1.25 <sup>+0.75</sup> <sub>-0.42</sub>	1 (fix)	1 (fix)	...	...	
Obs2(c)	10.8 <sup>+0.5</sup> <sub>-0.5</sub>	↑	↑	↑	↑	↑	↑	6.55 <sup>+0.23</sup> <sub>-0.09</sub>	1.5 <sup>+0.6</sup> <sub>-0.5</sub>	

<sup>†</sup> In units of photons keV<sup>-1</sup> cm<sup>-2</sup> s<sup>-1</sup> str<sup>-1</sup> @1keV.

<sup>‡</sup> In units of 10<sup>-3</sup> pccm<sup>-6</sup>.

<sup>§</sup> The emission measure of LHB+SWCX is fixed to 0.0033 pccm<sup>-6</sup> which corresponds to 1.0 LU of O VII K $\alpha$  emission as the estimated lower limit.

<sup>||</sup> The emission measure of LHB+SWCX is fixed to 0.0098 pccm<sup>-6</sup> which corresponds to 3.0 LU of O VII K $\alpha$  emission as the estimated lower limit.

background fluctuation due to the large-scale structure): e.g., due to the presence of a distant group/cluster of galaxies or two, which are too faint to be detected individually in the observation. The high-velocity clouds (HVCs) could be another candidate. Mkn 421 is projected inside the HVC Complex M. It is considered to be near the Galactic disk (Blitz et al. 1999), and may thus interact strongly with the hot ISM. The origin is still unknown because neither the distance nor the apparent size are known.

#### 4.2. Uncertainty due to the SWCX and LHB

The contamination from the geocoronal SWCX can be eliminated by screening the event data properly, but the heliospheric SWCX and LHB can not. Shadowing measurements show that the heliospheric SWCX and LHB contribute almost negligibly to the total above 500 eV, and their only effect on our analysis is their somewhat uncertain contribution of  $2 \pm 1$  LU to the measured O VII emission (Yoshino et al. 2009). We also performed a model simulation, which we developed for Yoshitake et al. (2013), according to Koutroumpa et al. (2006) and obtained the line intensities contributed from the heliospheric SWCX as 1.9 LU and 2.2 LU for solar minimum and solar maximum respectively, which are consistent with our estimation. We thus modeled the heliospheric SWCX and LHB using the parameter-fixed *mekal* to represent their O VII emission line.

We first obtained the best-fit and the lower and upper limits of LTC from the emission analyses using the lower and upper limits of the heliospheric SWCX and LHB O VII emission (Table 10). We then applied the obtained LTC temperatures to the joint fits (Table 11).

**Table 11.** Results from the spectral fits with the exponential model, together with the lower and upper limits to the SWCX and LHB contributions.

CXB		Hot ISM					LTC		$\chi^2/\text{dof}$
	Norm <sup>†</sup>	$v_b$	$\log T_0$	$\log(\gamma N_{\text{H}})$	$h_T$	$\gamma$	$\log T$	Norm <sup>‡</sup>	
		(km s <sup>-1</sup> )	(K)	(cm <sup>-2</sup> )	(kpc)		(K)		
LHB+SWCX = 1 LU <sup>§</sup> (Lower Limit)									
Exp(C)									545.77/518
Abs	...	59 <sup>+35</sup> <sub>-13</sub>	6.41 <sup>+0.09</sup> <sub>-0.08</sub>	19.00 <sup>+0.34</sup> <sub>-0.24</sub>	1.6 <sup>+2.2</sup> <sub>-0.9</sub>	0.39(< 1.60)	...	...	
Obs1	12.2 <sup>+0.5</sup> <sub>-0.6</sub>	...	↑	↑	↑	↑	...	...	
Obs2(c)	10.7 <sup>+0.5</sup> <sub>-0.5</sub>	...	↑	↑	↑	↑	6.63 (fix)	1.3 <sup>+0.3</sup> <sub>-0.3</sub>	
Exp(C); LTC Lower Limit									547.42/518
Abs	...	57 <sup>+28</sup> <sub>-8</sub>	6.47 <sup>+0.06</sup> <sub>-0.14</sub>	18.83 <sup>+0.47</sup> <sub>-0.14</sub>	1.3 <sup>+2.3</sup> <sub>-0.6</sub>	0.00(< 1.42)	...	...	
Obs1	12.1 <sup>+0.5</sup> <sub>-0.5</sub>	...	↑	↑	↑	↑	...	...	
Obs2(c)	10.8 <sup>+0.4</sup> <sub>-0.4</sub>	...	↑	↑	↑	↑	6.53 (fix)	1.6 <sup>+0.4</sup> <sub>-0.4</sub>	
Exp(C); LTC Upper Limit									548.75/518
Abs	...	58 <sup>+20</sup> <sub>-11</sub>	6.45 <sup>+0.05</sup> <sub>-0.06</sub>	18.88 <sup>+0.34</sup> <sub>-0.16</sub>	1.2 <sup>+1.0</sup> <sub>-0.6</sub>	0.11(< 0.77)	...	...	
Obs1	12.0 <sup>+0.5</sup> <sub>-0.5</sub>	...	↑	↑	↑	↑	...	...	
Obs2(c)	10.6 <sup>+0.5</sup> <sub>-0.5</sub>	...	↑	↑	↑	↑	6.81 (fix)	0.9 <sup>+0.2</sup> <sub>-0.2</sub>	
LHB+SWCX = 3 LU <sup>  </sup> (Upper Limit)									
Exp(C)									546.51/518
Abs	...	57 <sup>+29</sup> <sub>-9</sub>	6.46 <sup>+0.03</sup> <sub>-0.11</sub>	18.85 <sup>+0.48</sup> <sub>-0.14</sub>	1.4 <sup>+2.6</sup> <sub>-0.6</sub>	0.02(< 1.60)	...	...	
Obs1	12.1 <sup>+0.5</sup> <sub>-0.5</sub>	...	↑	↑	↑	↑	...	...	
Obs2(c)	10.8 <sup>+0.5</sup> <sub>-0.5</sub>	...	↑	↑	↑	↑	6.55 (fix)	1.5 <sup>+0.4</sup> <sub>-0.3</sub>	
Exp(C); LTC Lower Limit									553.45/518
Abs	...	62 <sup>+24</sup> <sub>-15</sub>	6.53 <sup>+0.07</sup> <sub>-0.09</sub>	18.77 <sup>+0.23</sup> <sub>-0.12</sub>	1.4 <sup>+1.5</sup> <sub>-0.8</sub>	0.00(< 0.46)	...	...	
Obs1	12.0 <sup>+0.6</sup> <sub>-0.5</sub>	...	↑	↑	↑	↑	...	...	
Obs2(c)	10.9 <sup>+0.5</sup> <sub>-0.5</sub>	...	↑	↑	↑	↑	6.46 (fix)	1.7 <sup>+0.5</sup> <sub>-0.4</sub>	
Exp(C); LTC Upper Limit									547.36/518
Abs	...	59 <sup>+36</sup> <sub>-13</sub>	6.44 <sup>+0.06</sup> <sub>-0.12</sub>	18.90 <sup>+0.34</sup> <sub>-0.18</sub>	1.2 <sup>+1.7</sup> <sub>-0.6</sub>	0.15(< 1.23)	...	...	
Obs1	12.0 <sup>+0.7</sup> <sub>-0.5</sub>	...	↑	↑	↑	↑	...	...	
Obs2(c)	10.6 <sup>+0.2</sup> <sub>-0.5</sub>	...	↑	↑	↑	↑	6.77 (fix)	0.9 <sup>+0.2</sup> <sub>-0.2</sub>	

<sup>†</sup> In units of photons keV<sup>-1</sup> cm<sup>-2</sup> s<sup>-1</sup> str<sup>-1</sup> @1keV.

<sup>‡</sup> In units of 10<sup>-3</sup> pccm<sup>-6</sup>.

<sup>§</sup> Emission measure of *mekal* for LHB+SWCX is set to 0.0033 pccm<sup>-6</sup>, which corresponds to 1.0 LU O VII K $\alpha$  emission as the estimated lower limit.

<sup>||</sup> Emission measure of *mekal* for LHB+SWCX is set to 0.0098 pccm<sup>-6</sup>, which corresponds to 3.0 LU O VII K $\alpha$  emission as the estimated upper limit.

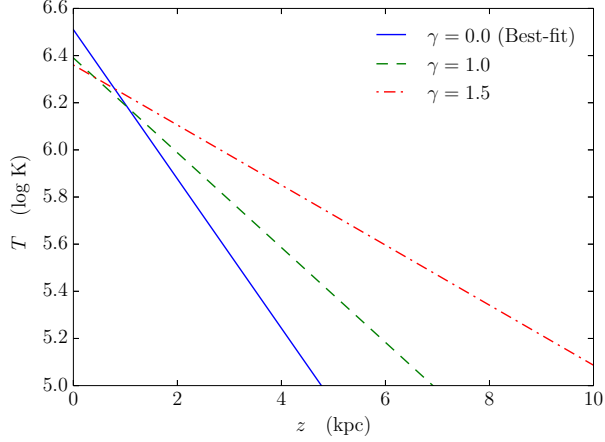


**Fig. 13.** Temperature drop along with the distance from the Galactic plane, predicted with the exponential model with the fixed LTC temperature and the thawed  $v_b$ , for the best-fitted  $\gamma$ , as well as for the unity scale height of density and temperature ( $\gamma = 1.0$ ) and the ideal gas ( $\gamma = 1.5$ ).

**Table 12.** 90% heights calculated from the density and the emission measure of the hot gas.

	Absorption		Emission	
	O VII	O VIII	O VII	O VIII
	(kpc)		(kpc)	
$\gamma = 0.0$ (Best-fit)	2.98	1.00	1.23	0.70
$\gamma = 1.5$ (Fixed)	4.70	1.39	1.43	0.84
$\gamma = 1.0$ (Fixed)	3.50	1.01	1.11	0.63

The results from the fits using the lower and upper limits are consistent with those from the fits using the typical line intensity for the heliospheric SWCX and LHB contributions.

#### 4.3. Distribution of the O VII and O VIII Emitting and Absorbing Gas

Assuming the exponential model, we obtained the temperature and hydrogen number density at the Galactic plane, as well as the scale heights. Figure 13 shows the temperature as a function of the distance from the Galactic plane under the best-fitted and the fixed  $\gamma$ -s (1 or 1.5 for the scale height ratio of density and temperature of an ideal gas). In any  $\gamma$ -s, the fitted results are consistent and the temperature scale heights take finite values less than 10 kpc. The velocity dispersions are also consistent with the thermal velocities ( $\sim 60$  km/s).

Using the fitted parameters, we calculated the oxygen number density (Figure 14) and the surface brightness (Figure 15) for O VII and O VIII emission lines as functions of the distance from the Galactic plane. We further computed the vertical heights at which the accumulated O VII and O VIII column density and surface brightness reach 90% of their totals (Table 12). In all cases, the obtained heights are less than 5 kpc.



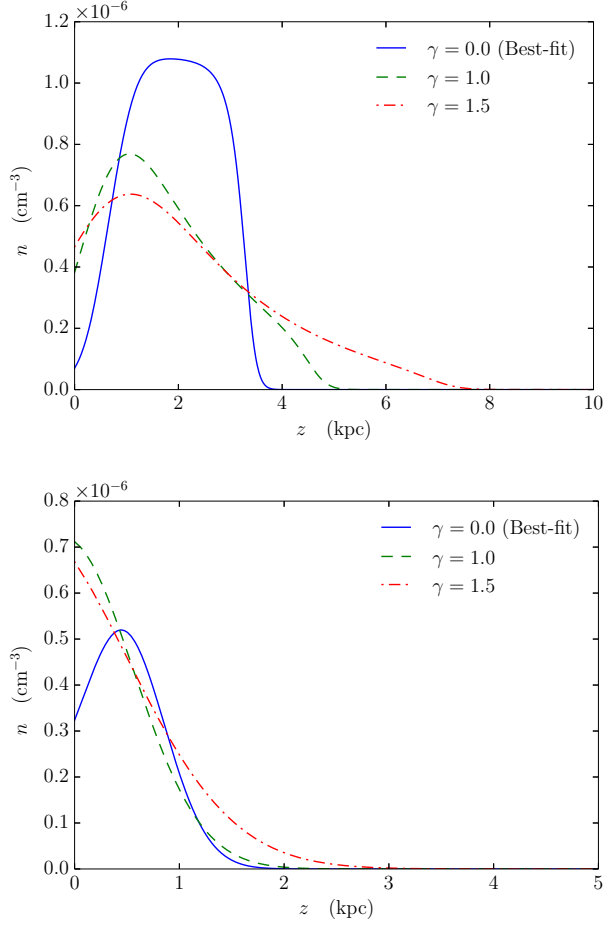


**Fig. 14.** Spatial distribution of the O VII (top) and O VIII (bottom) density as the functions of the distance from the Galactic plane, predicted with the exponential model, for the best-fitted and the fixed  $\gamma$ -s with the fixed LTC temperature and the thawed  $v_b$ , for the best-fitted  $\gamma$ , as well as for the unity scale height of density and temperature ( $\gamma = 1.0$ ) and the ideal gas ( $\gamma = 1.5$ ).

#### 4.4. Comparison with Other Works

Yao et al. (2009) and Hagihara et al. (2010) performed joint analyses of the absorption and emission spectra in the LMC X-3 and PKS 2155-304 directions and constrained the hot gas temperatures and densities at the plane together with the scale heights.

Here we compared our results with those directions (Table 13). The scale height  $h$  in the table represents the scale height for the temperature  $h_T$  for LMC X-3 and PKS 2155-304, and the scale height for the density  $h_n$  for Mkn 421, as we changed the parameter  $h_n$  of *vabmkl* to  $h_T$ . These values indicate a thick hot gas disk surrounding our Galaxy, which can be characterized by the exponential model of the column density, scale height and temperature:  $\sim 2 \times 10^{19} \text{ cm}^{-2}$ , a few kpc and  $\sim 2 \times 10^6 \text{ K}$ , respectively.

Gupta et al. (2012) combined an averaged column density from the *Chandra* absorption spectra with an averaged emission measure from literature and suggested that the spatial extent

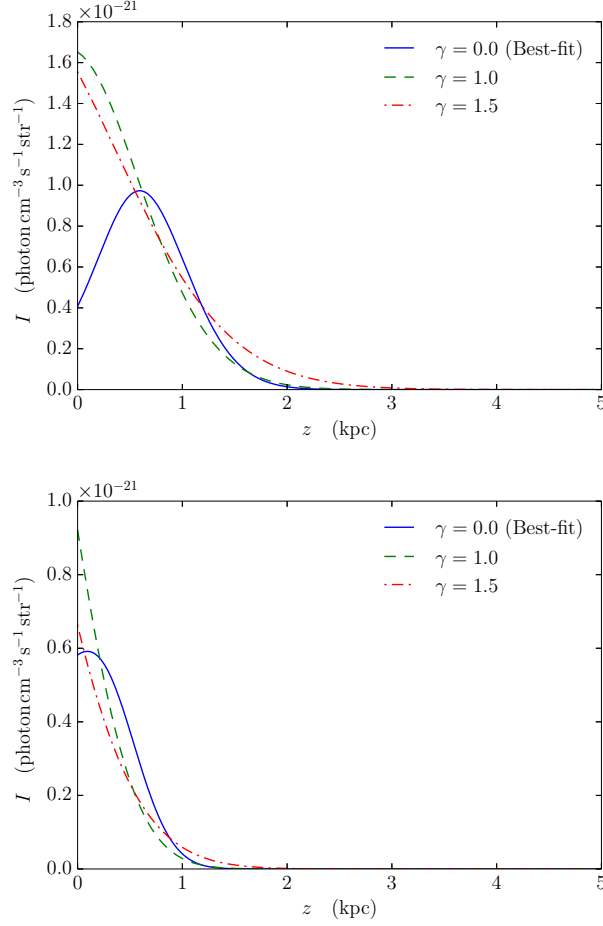


**Fig. 15.** Spatial distribution of the OVII (top) and OVIII (bottom) surface brightness as the functions of the distance from the Galactic plane, predicted with the exponential model with the fixed LTC temperature and the thawed  $v_b$ , for the best-fitted  $\gamma$ , as well as for the unity scale height of density and temperature ( $\gamma = 1.0$ ) and the ideal gas ( $\gamma = 1.5$ ).

of the hot gas is more than 100 kpc. Moreover, Gupta et al. (2013) combined the *Chandra* absorption spectra toward Mkn 421 with the same *Suzaku* emission spectra as we used in this paper, and claimed that the spatial extent and the density of the hot gas toward Mkn 421 are  $334^{+685}_{-274}$  kpc and  $(1.6^{+2.6}_{-0.8}) \times 10^{-4} \text{ cm}^{-3}$ , which differ by more than an order of magnitude from our results. These differences mainly come from the gas distribution model and the oxygen abundance. They assumed a uniformly distributed isothermal gas with  $0.2 Z_{\odot}$ , while we assumed the exponentially distributed gas with  $1 Z_{\odot}$ . Since  $EM \propto Zn^2L$  and  $CD \propto ZnL$ ,  $L \propto CD^2/(ZEM)$ , the difference in abundance therefore makes their spatial extent five time larger than our result. The difference in the distribution model also makes the extent differ. Since the gas temperatures obtained from the absorption line analysis and the emission line analysis are inconsistent, as with previous studies in two other directions, a model with temperature variation along the vertical distance from the Galactic plane is more appropriate than an

**Table 13.** Obtained exponential model parameters with LMC X-3 and PKS 2155–304 sight lines.

Direction	$(\ell, b)$ ( $^{\circ}$ )	$\log T_0$ (K)	$\log N_{\text{H}_{\text{Hot}}}$ ( $\text{cm}^{-2}$ )	$h^{\dagger}$ (kpc)	$\gamma$
Mkn 421	(179.8, 65.0)	$6.51^{+0.07}_{-0.12}$	$18.80^{+0.31}_{-0.14}$	$1.6^{+1.7}_{-0.7}$	$0.00(< 0.74)$
LMC X-3	(273.6, -32.1)	$6.56^{+0.11}_{-0.10}$	$19.36^{+0.22}_{-0.21}$	$2.8^{+3.6}_{-1.8}$	$0.5^{+1.2}_{-0.4}$
PKS 2155–304	(17.7, -52.2)	$6.40^{+0.09}_{-0.05}$	$19.10^{+0.08}_{-0.07}$	$2.3^{+0.9}_{-0.8}$	$2.44^{+1.11}_{-1.41}$

 $^{\dagger} h_n$  for LMC X-3 and PKS 2155–304, and  $h_T$  for Mkn 421.

isothermal model. In this paper, we adopted the exponential model that the temperature and density decrease exponentially with the vertical distance from the Galactic plane. As for the hot gas observable by highly ionized oxygen, our results are consistent with observations of highly ionized absorption lines in spectra of Galactic sources (e.g., Futamoto et al. 2004) indicating that most of hot gas contributing to the absorption exists within distance scales of  $\sim 10$  kpc.

## 5. Summary

We have jointly analyzed X-ray absorption and emission spectral observed by *Chandra* and *Suzaku* to study the structure of the hot ISM along the sight line toward Mkn 421. Our main results and conclusions are summarized as follows:

1. We have detected O VII and O VIII lines in the emission spectra from two *Suzaku* observations taken in the fields adjacent to the Mkn 421 sight line. The two spectra show significant difference, indicating a patchy thermal emission component to Obs2 spectrum. By modeling these emission spectra (excluding local contributions), we obtained a characteristic temperature of the emitting gas as  $(2.0^{+0.2}_{-0.3}) \times 10^6$  K, assumed to be isothermal and in the CIE. This temperature is about 30% higher than that of the absorption gas under the same assumption.
2. We have jointly analyzed the *Chandra* absorption and *Suzaku* emission spectra adopting the exponential thick Galactic hot gas disk model, and found that obtained the gas temperature and the density to be  $(3.2^{+0.6}_{-0.7}) \times 10^6$  K and  $(1.2^{+0.5}_{-0.4}) \times 10^{-3} \text{ cm}^{-3}$  at the Galactic plane and have the scale heights of  $1.6^{+1.7}_{-0.7}$  kpc and  $> 2.8$  kpc, respectively.
3. The results we have obtained from these joint analysis are consistent with those for the LMC X-3 and PKS 2155–304 directions, consistent with the presence of the thick hot gas disk with a vertical scale height of a few kpc.

YY acknowledges financial support by NASA through ADP grant NNH12CG14C to Eureka Scientific, while QDW is supported by NASA via grant NNX10AE85G.

## References

- Anders, E., & Grevesse, N. 1989, *Geochim. Cosmochim. Acta*, 53, 197
- Berkhuijsen, E. M., Haslam, C. G. T., & Salter, C. J. 1971, *A&A*, 14, 252
- Bregman, J. N., & Lloyd-Davies, E. J. 2007, *ApJ*, 669, 990
- Cox, D. P. 1998, in *Lecture Notes in Physics* (Berlin: Springer Verlag), 506, 121
- Blitz, L., Spergel, D. N., Teuben, P. J., Hartmann, D. & Burton, W. B. 1999, *ApJ*, 514, 818
- Cox, D. P. 2005, *ARA&A*, 43, 337
- Cravens, T. E. 2000, *ApJ*, 532, L153
- Fang, T., McKee, C. F., Canizares, C. R., & Wolfire, M. 2006, *ApJ*, 644, 174
- Fang, T., Bullock, J. & Boylan-Kolchin, M. 2013, *ApJ*, 762, 20
- Ferrière, K. 1998, *ApJ*, 497, 759
- Fujimoto, R., et al. 2007, *PASJ*, 59, S133
- Futamato, K., Mitsuda, K., Takei, Y., Fujimoto, R., & Yamasaki, N. Y. 2004, *ApJ*, 605, 793
- Galeazzi, M., Gupta, A., Covey, K., & Ursino, E. 2007, *ApJ*, 658, 1081
- Gupta, A., Nicastro, F. & Galeazzi, M. 2012, *ApJL*, 756, L8
- Gupta, A., Mathur, S., Galeazzi, M., & Krongold, Y. 2013, *arXiv:1307.6195*
- Hagihara, T., Yao, Y., Yamasaki, N. Y., Mitsuda, K., Wang, Q. D., Takei, Y., Yoshino, T., & McCammon, D. 2010, *PASJ*, 62, 723
- Henley, D. B., Shelton, R. L., & Kuntz, K. D. 2007, *ApJ*, 661, 304
- Ishisaki, Y., et al. 2007, *PASJ*, 59, 113
- Juett, A. M., Schulz, N. S., Chakrabarty, D. & Gorczyca, T. W. 2006, *ApJ*, 648, 1066
- Kalberla, P. M. W., Burton, W. B., Hartmann, D., Arnal, E. M., Bajaja, E., Morras, R., Pöppel, W. G. L. 2005, *A&A*, 440, 775
- Kharchenko, V., Rigazio, M., Dalgarno, A., & Krasnopolsky, V. A. 2003, *ApJL*, 585, L73
- Koutroumpa, D., Lallement R., Kharchenko V., Dalgarno A., Pepino R., Izmodenov V., & Quémerais E. 2006, *A&A*, 460, 289
- Koutroumpa, D., Acero, F., Lallement, R., Ballet, J., & Kharchenko, V. 2007, *A&A*, 475, 901
- Koyama, K., et al. 2007, *PASJ*, 59, 23
- Kuntz, K. D., Snowden, S. L. 2008, *ApJ*, 674, 209
- Lallement, R., Raymond, J. C., Vallergera, J., Lemoine, M., Dalaudier, F., & Vertaux, J. L. 2004, *A&A*, 426, 875
- Li, J.-T., Li, Z., Wang, Q. D., Irwin, J. A., & Rossa, J. 2008, *MNRAS*, 390, 59
- Masui, K., Mitsuda, K., Yamasaki, N. Y., Takei, Y., Kimura, S., Yoshino, T., & McCammon, D. 2009, *PASJ*, 61, 115
- McCammon, D., & Sanders, W. D. 1990, *A&A*, 28, 657
- McCammon, D., et al. 2002, *ApJ*, 576, 188
- Miller, E. D., et al. 2008, *PASJ*, 60, 95
- Miller, M. J. & Bregman, J. N. 2013, *ApJ*, 770, 118
- Mitsuda, K., et al. 2007, *PASJ*, 59, 1
- Morrison, R., & McCammon, D. 1983, *ApJ*, 270, 119
- Norman, C. A., & Ikeuchi, S. 1989, *ApJ*, 345, 372

- Sembach, K. R., Savage, B. D., Tripp, T. M. 1997, *ApJ*, 480, 216
- Serlemitsos P. J., et al. 2007, *PASJ*, 59, 9
- Shelton, R. L., Shallmen, S. M., & Jenkins, E. B. 2007, *ApJ*, 659, 365
- Smith, R. K., et al. 2007, *PASJ*, 59, S141
- Snowden, S. L., McCammon, D. & Verter, F., *ApJ*, 409, L21
- Snowden, S. L., Egger, R., Freyberg, M. J., McCammon, D., Plucinsky, P. P., Sanders, W. T., Schmitt, J. H. M. M., Trümper, J., & Voges, W. 1997, *ApJ*, 485, 125
- Strickland, D. K., Heckman, T. M., Colbert, E. J. M., Hoopes, C. G., & Weaver, K. A. 2004, *ApJS*, 151, 193
- Sutherland, R. S., & Dopita, M. A. 1993, *ApJS*, 88, 253
- Takei, Y., Akamatsu, H., Hiyama, Y., Maeda, Y., Ishida, M., Mori, H., Ishisaki, Y., & Hoshino, A. 2012, *AIP Conf. Proc.*, 1427, 239
- Tawa, N. et al. 2008, *PASJ*, 60, S22
- Williams, R. J., et al. 2005, *ApJ*, 631, 856
- Wang, Q. D., Immler, S., Walterbos, R., Lauroesch, J. T., Breitschwerdt, D. 2001, *ApJL*, 555, 99
- Wang, Q. D., Chaves, T., Irwin, J. D. 2003, *ApJ*, 598, 969
- Wang, Q. D. & Yao, Y. 2012, *arXiv*, 1211, 4834
- Yamasaki, N. Y., Sato, K., Mitsuishi, I., & Ohashi, T. 2009, *PASJ*, 61, 291
- Yao, Y., & Wang, Q. D. 2005, *ApJ*, 624, 751
- Yao, Y., & Wang, Q. D. 2006, *ApJ*, 641, 930
- Yao, Y., & Wang, Q. D. 2007, *ApJ*, 658, 1088
- Yao, Y., Nowak, M. A., Wang, Q. D., Schulz, N. S. & Canizares, C. R. 2008, *ApJL*, 672, 21
- Yao, Y., Wang, Q. D., Hagihara, T., Mitsuda, K., McCammon, D., & Yamasaki, N. Y. 2009, *ApJ*, 690, 143
- Yao, T., Shull, J. M., & Danforth, C. W. 2011, *ApJL*, 728, 16
- Yoshino, T., et al. 2009, *PASJ*, 61, 805
- Yoshitake, H., et al. 2013, *PASJ*, 65, 32